ISSN 1392-1207. MECHANIKA. Vol. 31, No. 1, 2025: 27–34

Shape Optimization of the Aerostatic Bearing Considering Dynamic Performances

Yifei LI
School of Civil and Transportation Engineering, Qinghai Minzu University, Xining 810001, China,
E-mail: liyifei@buaa.edu.cn

https://doi.org/10.5755/j02.mech.36754

1. Introduction

The aerostatic bearings play an important role in the ultra-precision manufacturing fields. The bearing mechanical performances have a significant influence on behaviour of the ultra-precision facilities; consequently, they should be improved in the bearing design stage. Especially, the bearing dynamic performances relating to the operational stability should be paid more attention.

Commonly, the concentrated bearing performances include the static and the dynamic performances, respectively. The static performances generally contain the static load carrying capacity and the static stiffness; these performances are in-depth studied and fully considered in the bearing design [1-4]. While for the dynamic performances, the difficulties in both solution and mechanism analysis bring trouble to the bearing design. Due to the importance of the bearing operational stability, not only the dynamic characteristics such as the stiffness and damping, but also the self-excited excitation characteristics have been studied. In analysis of the stiffness and damping, the air film is regarded as a spring-damping system [5]. Commonly, the stiffness and damping can be achieved by either solving the perturbed Reynolds equation [6-7] or conducting the numerical simulation directly [8]. Besides, to improve the bearing operational stability, the self-excited excitation should also be studied. The self-excited excitation can induce the micro-vibration or the pneumatic hammering vibration, and weaken the bearing operational stability greatly. Thus, the self-excited excitation is imperative to be suppressed. The researches revealed that the micro-vibration was induced by occurrence of the vortex flow in the bearing clearance [9-10]. The reason was that when the vortex flow occurred, the pressure distribution in the flow field became unsteady, which caused the fluctuation of the load carrying force, and thence, the micro-vibration was induced. Besides, the pneumatic hammering is induced by asynchronous variation of the pressure, motion and gas mass flow rate with time [11]. To reduce the micro-vibration, the suppression of the vortex flow is crucial [12-13]. For the aerostatic bearing with non-pocket orifice type restrictor, the existence of the supersonic region and the shock waves may cause the separation of boundary layer and then induce the vortex flow [14]. While for the bearing with pocketed orifice type restrictor, the air pocket offers a large volume for development of the vortexes, and hence, the micro-vibration is more serious compared with the non-pocket case. It indicates that reducing the Reynolds number at the inlet of the pocket is conducive for suppressing the micro-vibration [10]. For suppressing of the pneumatic hammering vibration, it showed that the volume of the air pocket and the air supply pressure should both be limited [15]. The mechanical performances of the aerostatic bearings are greatly influenced by the shape and volume of the air pocket. Ye et.al [15] indicated that with larger pocket volume, the pneumatic hammering vibration was prone to occur. Chen et.al. [9] investigated the effects of the air pocket shape and volume on the micro-vibration, and it showed that the micro-vibration amplitude increased with the pocket volume. In GAOs' research [16], influences of several pocket shapes on performances of the aerostatic thrust bearing were compared. Commonly, with the larger pocket volume, the aerostatic bearings have better static performances, while the dynamic performances are weakened, and the self-excited excitation vibration is prone to occur. Hence, it is necessary to balance the static and dynamic performances in selection of the air pocket. For this purpose, the multi-objective optimization is always considered [17-18]; the optimization parameters commonly include the geometry and the operation parameters. Due to the great influence of the air pocket shape on performances [19], the multi-objective shape optimization is necessary to be prepared. However, the optimization model considering both static and dynamic performances has not been referred yet; the optimization objectives considered currently are generally the static performances, while the dynamic performances are seldom considered. Considering both static and dynamic performances in design optimization can certainly enhance the bearing performances further.

In this study, the shape optimization of the air pocket is conducted. Firstly, a basic configuration of the air pocket is proposed and the bearing parameters selected for optimization are determined. And then, the flow field in the bearing clearance is researched, and several typical flow structures are discussed in detail; the dynamic characteristics are studied and the displacement impedance of the air film-floating facility system is selected as one of the optimization objective. Finally, the optimization model is established and both the static and the dynamic performances are taken into account. The optimizations have been conducted under several given bearing loads, and the results are compared and discussed. The effects of air pocket shape and volume on dynamic performances are further discussed.

2. Basic Configuration of the Air Pocket for Shape Optimization

An aerostatic bearing with orifice-type restrictor as shown in Fig. 1 is considered for optimization, where Φ is bearing diameter, U is the diameter of the air pocket, d is

the orifice diameter, and h is the air film thickness. Different pockets such as the non-pocket, the cylindrical pocket and the tapered pocket can be considered in the bearing design. Generally, when a larger pocket volume is adopted, although the static performances can be improved, the risk of the self-excited vibration also increases. Hence, the design optimization is essential to achieve the proper pocket shape and volume.

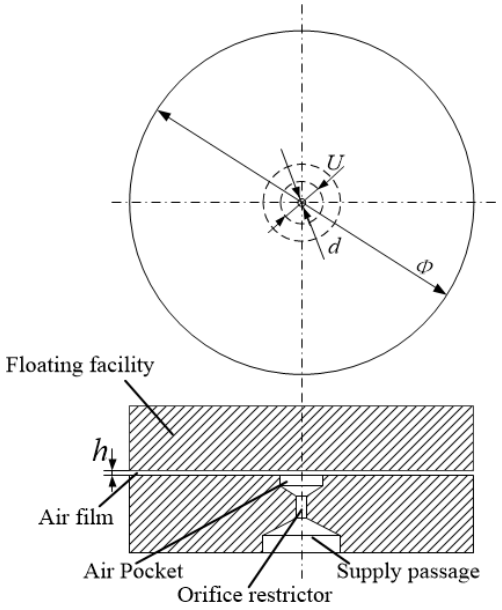

Fig. 1 The aerostatic bearing with orifice-type restrictor

In this study, the pocket configuration as shown in Fig. 2 is established. Where l denotes the orifice length, V_1 and V_2 are the pocket depth. Φ equals 50 mm and l equals 0.5 mm, other geometry parameters are considered as design variables. In optimization, the variable ranges include: U [0.1 mm, 1.1 mm], V_1 [0.05 mm, 0.15 mm], V_2 [0 mm, 0.1 mm], d [0.1 mm, 0.2 mm]. The air supply pressure P_s is also taken as a design variable, and the range is [0.45 MPa, 0.7 MPa]. Such an air pocket configuration is especially practicable in the shape optimization. When V_2 equals 0mm, the pocket turns into a cylindrical pocket; while when U equals d, the non-pocket case is achieved. Also, when V_1 becomes rather small, the pocket can be regarded as a tapered pocket. Different optimization cases are considered and the influences of the air pocket on mechanical performances are further discussed later.

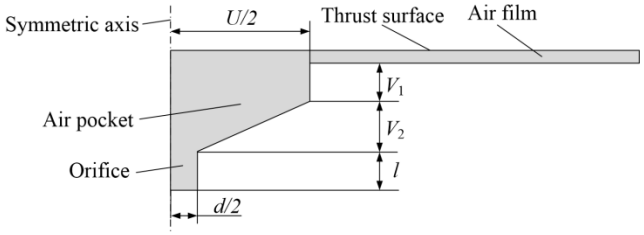

Fig. 2 The basic configuration of the air pocket for optimization

A three-dimensional model (3D model) is established for the numerical simulation, and the numerical model is shown in Fig. 3. Due to the symmetrical properties, only 1/12 of the whole model is considered for simplicity. Although the two-dimensional symmetric model is applicable for calculations, employing a three-dimensional model enables a more accurate simulation of the vortex structures in the flow field of the bearing clearance. The three-dimensional model contributes to greater precision in the computation of bearing performances.

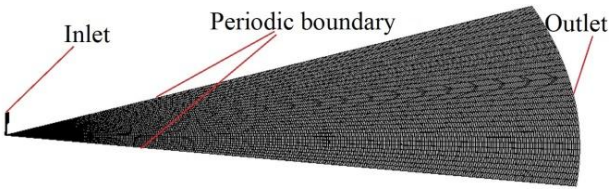

Fig. 3 The numerical model of the bearing flow field

At the inlet of the air supply passage, the pressure inlet boundary condition is applied and the pressure is the air supply pressure; at the outlet of the air film, the pressure outlet condition is adopted and the pressure equals the atmospheric pressure; the adjacent surfaces of the air film part with other parts are set as periodic boundary. Other surfaces such as the thrust surface, the orifice and pocket surfaces are all considered as walls which satisfy non-slip conditions. The large eddy simulation (LES) model is applied in the numerical simulation to achieve the accuracy vortex structure, and the governing equations are solved numerically by using the computational fluid dynamics (CFD) method. The equations include the continuity equation, the momentum equations and the energy equation.

3. Typical Flow Structure of The Bearing Clearance with Different Air Pocket

Varying either the shape or the volume of the pocket, the bearing mechanical performances become entirely different. It indicated that with the smaller air pocket, the load carrying capacity was weakened while the risk of the self-excited excitation was reduced. For the pocket configuration discussed in Fig. 2, four typical flow patterns are observed. For example, Case 1: h = 12 μm, d = 0.1 mm, U = 0.1 mm, V_1 = 0.05 mm, V_2 = 0.05 mm; Case 2: h = 12 μm, d = 0.1 mm, U = 0.2 mm, V_1 = 0.1 mm, V_2 = 0.05 mm; Case 3: h = 12 μm, d = 0.1 mm, U = 1 mm, V_1 = 0.05 mm, V_2 = 0.1 mm; Case 4: h = 12 μm, d=0.1 mm, U = 1 mm, V_1 = 0.1 mm, V_2 = 0 mm. When P_s equals 0.1 MPa, the flow structures are shown in Fig. 4, where the gas velocity stays subsonic in all cases.

For the non-pocket situation as Case 1, when the air flows out of the orifice, it forms the air film immediately. When the air supply pressure is low, there is no supersonic region. Due to the sudden change of the flow direction, a separation bubble occurs at the inlet region of the air film; the effective area of the flow section is reduced and the flow velocity increases, and as a result, the largest gas velocity occurs at the inlet position of the air film. For Case 2, a small air pocket is added at the outlet of the orifice. For this case, a jet flow forms at the inlet of the pocket, while it is prevented by the thrust surface. However, because the volume of the air pocket is rather small for development of the vortex flow, the formed vortexes do not flow downstream and only a separation bubble is observed in the pocket. The flow structure in the air film is similar with that of the non-pocket case. For Case 3, a larger tapered pocket is adopted, and for Case 4, a

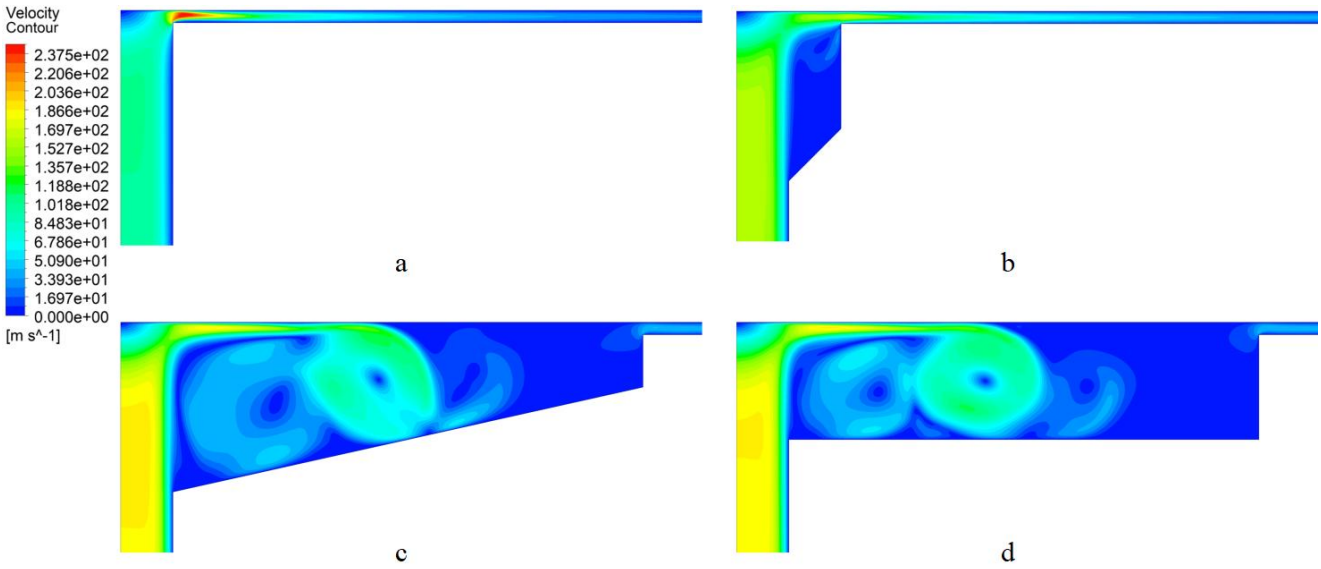

Fig. 4 The subsonic flow structure in the bearing flow field: a – Case 1, b – Case 2, c – Case 3, d – Case 4

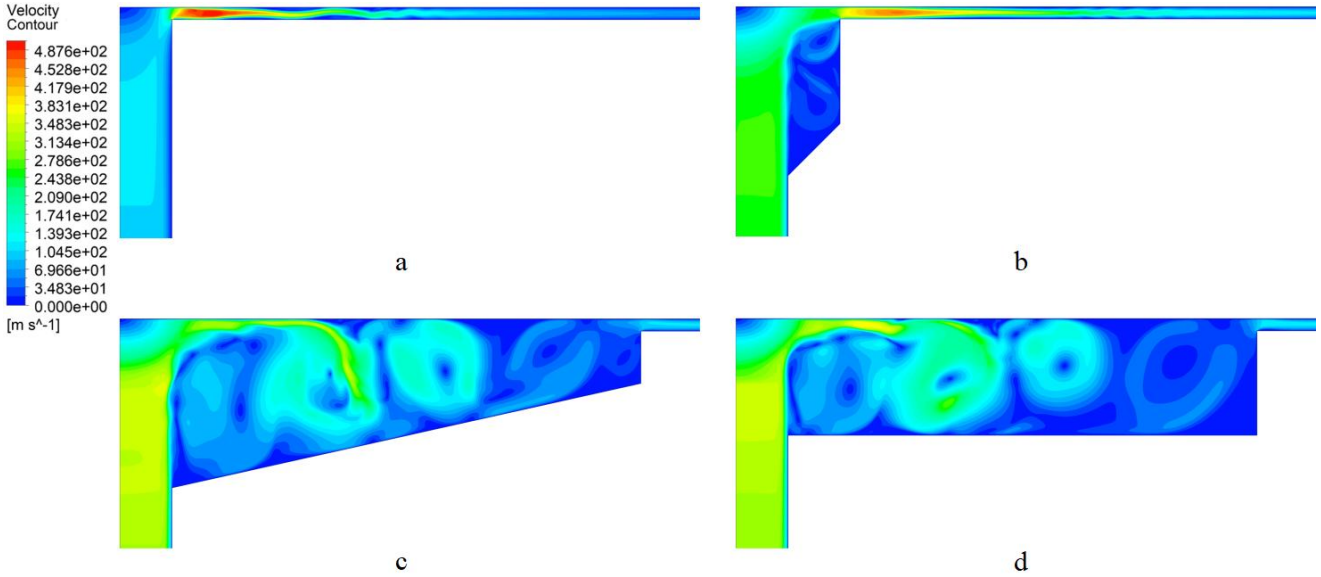

Fig. 5 The supersonic flow structure in the bearing flow field: a – Case 1, b – Case 2, c – Case 3, d – Case 4

cylindrical pocket is used. The flow structures of Case 3 and Case 4are similar. For Case 3 and 4, the pocket volume is far larger than that of the orifice, and the jet flow forms at the inlet of the pocket. When the gas flows into the air pocket and hits the upper thrust surface, its direction turns and the vortexes form; as the pocket offers enough volume for development of the vortexes, the vortexes form continuously and flow along the bearing radial direction, and finally, disappear due to the viscous dissipation and the reduction of the gas velocity. It can be concluded that for the non-pocket or the small pocket cases, when the gas velocity is lower than the sound velocity, the vortex flow is not detected and only the separation bubble is observed in the small pocket. However, when the pocket is large enough, the vortexes can be detected in both tapered and cylindrical pocket cases. When the vortex flow occurs in the bearing clearance, the pressure fluctuates with time; it is due to the fact that the pressure is disturbed by the always existed low pressure point in the center of a vortex. As a result of the pressure fluctuation, the load carrying force is fluctuating correspondingly and the micro-vibration is induced. In other word, the formation of the vortex flow is harm to the bearing operational stability.

Once the supersonic region occurs, the flow structure becomes more complicated. When the air supply pressure increases to 0.7 MPa, the supersonic region occurs as shown in Fig. 5. It can be seen that for the non-pocket case, the Mach number reaches to 1.8. The supersonic region occurs at the inlet of the air film, as discussed in [14]; due to the sudden change of the flow direction at the inlet of the air film and the interaction between the gas flow and the separation bubble, the Mach waves, i.e. the expansion waves, may occur at the beginning of the supersonic region, which further raise the gas velocity. And due to the interaction between the gas flow and the bearing surfaces, the shock wave forms at the end of the supersonic region which results in the flow separation. As a result, the vortex flow forms. For Case 2, the separation bubble is also detected in the small pocket, and the supersonic region occurs at the inlet of the air film; the flow structure at the inlet of the air film is similar with that of the non-pocket case. Consequently, it can be concluded that the supersonic

region accompanied with the shock waves is the main cause of the vortex flow. For Case 3 and 4, the flow structures are similar with those of the subsonic cases. Due to the increase of the boundary layer thickness in the orifice, the effective area of cross section of the flow channel is reduced. While when the gas flows into the pocket, the jet boundary deflects, which increases the effective area of cross section of the flow channel. Hence, the supersonic region may form as the same with a Laval nozzle. The expansion waves may appear at the inlet of the pocket, and also, the shock waves may occur at the end of the supersonic region. However, the vortex flow always forms as the same with the subsonic cases for Case 3 and Case 4.

It can be seen from Fig. 4 and Fig. 5 that for the non-pocket case, when the gas velocity stays subsonic, the vortex flow is not observed, while when the supersonic region occurs at the inlet position of the air film, the vortex flow may form downstream. When a small pocket is used, separation bubbles are observed in the pocket, but these separation bubbles do not flow downstream along the radial direction, so the vortex flow is not observed. Hence, for suppressing the micro-vibration of the bearing without a pocket or with a small pocket, it is necessary to eliminate the supersonic region, i.e. the maximum Mach number in the flow should be less than 1. While for the tapered pocket case and the cylindrical pocket case, the vortex flow always exists whether or not the supersonic region occurs; due to the ever-present vortex flow, the micro-vibration is hard to be eliminated completely. However, in such cases, the Reynolds number at the inlet of the pocket can be reduced to weaken the micro-vibration [10]. In general, the maximum Mach number and the Reynolds number should both be considered in the shape optimization to reduce the micro-vibration.

4. Analysis of the Displacement Impedance

To improve the bearing operational stability, the self-excited excitation should first be reduced. Moreover, the dynamic characteristics such as the stiffness and the damping of the air film are concentrated [5, 8]. However, only considering the stiffness and the damping is not enough for the bearing to improve the load-resistance capability. Hence, in this research, the displacement impedance performance of the air film-floating facility system is considered in optimization for improving the bearing operational stability.

Once the air film is regarded as a spring-damping system, and when the floating facility is subjected to a harmonic excitation, the dynamic equation can be represented as:

$$m\ddot{x} + C\dot{x} + Kx = F_0 e^{i\omega t}, \tag{1}$$

where m is the mass of the floating facility, C is the air film damping, K is the air film stiffness, F_0 is the amplitude of the external dynamic force and ω is the excitation frequency. The displacement x has the same frequency as that of the excitation force. Hence, x can be expressed as:

$$x = X_0 e^{i\omega t}, \tag{2}$$

where X_0 is the amplitude of the displacement. Substituting Eq. (2) into Eq. (1), and the displacement impedance can be achieved as:

$$|Z| = |F_0 / X_0| = \sqrt{(K - m\omega^2)^2 + (C\omega)^2}. \tag{3}$$

It can be seen from Eq. (3) that with the larger displacement impedance, the smaller displacement amplitude can be achieved. In other words, the displacement impedance reflects the capability of the bearing to resist the dynamic excitation. Consequently, the displacement impedance is also taken as a design objective in optimization. Due to the squeeze film effect [20], the stiffness and the damping of the air film are highly depending on the excitation frequency, and as Eq. (3), the displacement impedance is also influenced by the excitation frequency. In calculation of the displacement impedance, firstly the stiffness and damping are both calculated numerically, and then the displacement impedance is determined by using Eq. (3). The dynamic mesh method is adopted in numerical simulation, and a sinusoidal time-dependent displacement excitation is imposed on the thrust surface. The air film is equivalent to a spring-damping system and both the stiffness and damping are calculated based on the relationship between the input displacement excitation and the output dynamic force. In application of the dynamic mesh method, the SIMPLE algorithm is considered and the layering method is used. 100 time steps are considered over one time period. The load carrying force varies with time, and its time-average value equals the static load carrying capacity actually. In order to verify the calculation accuracy of the numerical simulation, the experiments conducted in [14] are considered for comparison. In [14], an aerostatic bearing with a non-pocket orifice-type restrictor was analysed. The bearing has a diameter of 50 mm, an orifice diameter of 0.1 mm, and an air supply pressure of 0.4 MPa. In [14], the static load-carrying capacity was both experimentally measured and numerically simulated, and the results were compared. However, in this study, the dynamic load-carrying capacity is investigated, and the time-averaged value of the dynamic load-carrying capacity is compared with the experimental results from [14]. It is expected that the time-averaged value of the dynamic load-carrying capacity should match the experimentally obtained static load-carrying capacity. Firstly, the excitation frequency is set to 1000 Hz, and the average value of the dynamic load-carrying force $\overline{W}$ is calculated numerically. Additionally, two types of grids are considered for comparison: in the fine mesh case, the mesh density along the air film thickness is twice that of the coarse mesh case. As shown in Fig. 6, the numerical results agree well with the experimentally obtained values, demonstrating the accuracy of the numerical simulation. Furthermore, the numerical simulation is mesh-independent.

The accuracy of the displacement impedance solution is closely related to the calculation of bearing stiffness and damping. Therefore, the calculation accuracy of the frequency-dependent dynamic stiffness and damping should also be verified. The simulation results for stiffness have been compared with experimental data in our previous work [21], where the experimental results are sourced from [20]. The numerical simulation results show good agreement with the experimental results.

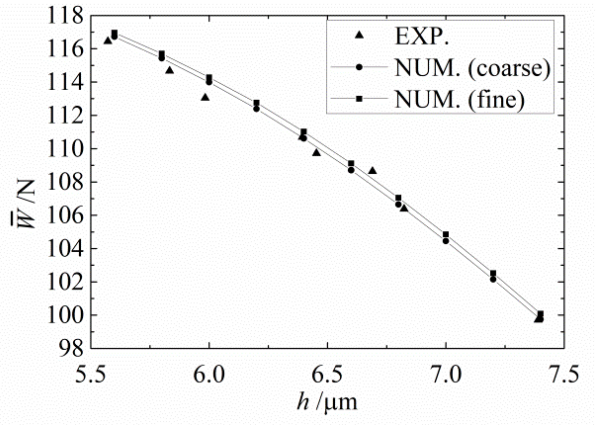

Fig. 6 Comparison between the numerical and experimental load carrying force

To have a further insight into the effects of bearing parameters on displacement impedance, the approximate model of displacement impedance represented by bearing parameters is established. The radial basis functions (RBF) method is used to achieve a high precision analysis model. The basic RBF model is expressed as Eq. (4).

$$Z(\boldsymbol{x}) = \sum_{s=1}^{N} \alpha_s \phi_s(\boldsymbol{x}) + \alpha_{N+1}, \tag{4}$$

where $\phi_s(\boldsymbol{x}) = \phi(\| \boldsymbol{x} - \boldsymbol{x}_s \|) = \| \boldsymbol{x} - \boldsymbol{x}_s \|^c \quad (s = 1, 2, \cdots, N)$ is the radial basis function, c is the shape function factor, $Z(\boldsymbol{x})$ is the interpolation function; α_1, α_2, …, α_{N+1} are interpolation expansion coefficients which should be determined firstly.

Once the sample points x_r (r = 1, 2, …, N) are selected, the sampling values y_r are calculated based on the selected sample points, and Eq. (5) is calculated to achieve α_1, α_2, …, α_{N+1} based on Eq. (4) as:

$$\begin{cases} \sum_{s=1}^{N} \alpha_s \phi_s(\boldsymbol{x}_r) + \alpha_{N+1} = y_r \quad , r = 1, \ \ldots, \ N, \\ \sum_{s=1}^{N} \alpha_s = 0 \ . \end{cases} \tag{5}$$

Each design variable should be normalized firstly, and the fitting accuracy of the approximate model is verified by using the R_α^2 factor, which should be larger than 0.9. In this research, the displacement impedance Z, the maximum Mach number M_a, the Reynolds number at the inlet R_e, and the load carrying capacity W are all considered in the optimization, and consequently, the approximate model of these performances are established. The considered parameters are d, h, V_1, V_2, U, P_s, ω for Z, and d, h, V_1, V_2, U, P_s for W, M_a and R_e. A layout $L_{121}(11^7)$ is established based on the orthogonal experimental design, and 121 sets of numerical simulation have been launched for sample taking. The ranges of the bearing parameters have been discussed in section 2. Once the approximate model is established, the relationship between the bearing performance and the parameters is known. As discussed above, M_a and R_e are highly related to the micro-vibration. Commonly, when the air film thickness increases, the air-resistance is reduced, and both the maximum Mach number and the Reynolds number increase. Similarly, M_a and R_e both increase with the air supply pressure. However, the variation of M_a or R_e with the pocket shape and sizes is non-monotonic, so a shape optimization should be conducted. When h= 10 μm, d = 0.1 mm, and P_s = 0.6 MPa, the variation of M_a with respect to V_1 and V_2 under different U is shown in Fig. 7. Also, the variation of R_e with these parameters is shown in Fig. 8. Three pocket diameters are discussed in Fig. 7 and Fig. 8, and the case U = 0.1 mm indicates a non-pocket situation.

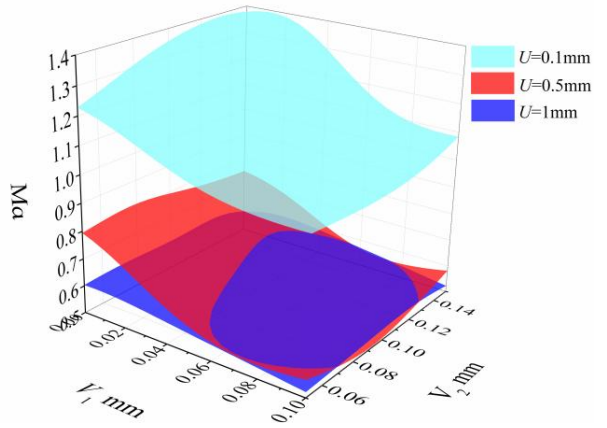

Fig. 7 Variation of maximum Mach number with respect to pocket sizes

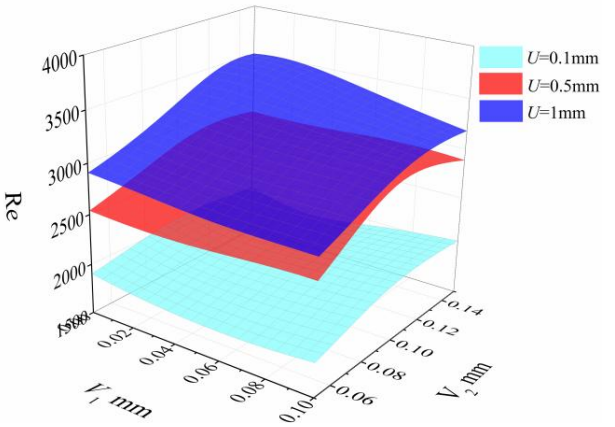

Fig. 8 Variation of Reynolds number at the inlet with respect to pocket sizes

It can be seen that with a larger pocket, although the maximum Mach number tends to be smaller, the Reynolds number becomes larger. Once a pocket is used, it indicates that the vortex-excitation is more serious. While for the non-pocket case, although the Reynolds number is lower, the supersonic region may exist and the vortex flow can form when the Mach number is larger than the sound speed. As a result, R_e and M_a should be considered in the optimization both.

When d = 0.1 mm, and P_s = 0.6 MPa, the variation of displacement impedance Z with respect to h and ω can be seen in Fig. 9. Three different pockets are considered for comparison: for Case 1, U = 0.1 mm, V_1 = 0.05 mm and V_2=0mm, which represents the non-pocket case; for Case 2, U = 0.5 mm, V_1 = 0.1 mm and V_2 = 0.1 mm, which represents the tapered pocket case; for Case 3, U = 1 mm,

$V_1 = 0.15$ mm and $V_2 = 0$ mm, which represents the cylindrical pocket case.

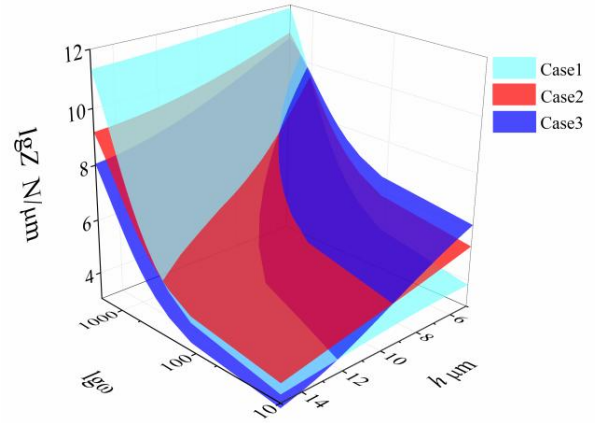

Fig. 9 Variation of displacement impedance with respect to pocket sizes

As discussed above, the displacement impedance represents the capability of the bearing to resist the dynamic load. It can be seen that the displacement impedance increases fast with the excitation frequency, and it is due to the well-known "squeeze film" effect: when the floating facility is subjected to external excitation with high frequencies, the air film becomes stiffer, and meanwhile, the inertial force of the floating facility becomes rather large. In other words, the bearing can resist the excitation with high frequencies effectively. Thereby, the excitation with low frequencies should be paid more attention in the bearing design, e.g., when the frequency is lower than KHz-order. Actually, the vortex-induced excitation can be regarded as a combination of a series of harmonic components with different frequencies; to reduce the vortex-induced excitation, and thus suppressing the micro-vibration, the displacement impedance at low frequencies should be especially considered in optimization [21]. For both the micro-vibration and the pneumatic hammering vibration, the vibration frequency is commonly at KHz-order [12], which indicates that the displacement impedance in this frequency range should be particularly concentrated. It can be seen from Fig. 9 that with decrease of the air film thickness, the displacement impedance increases; it means that the decrease of the air volume in the bearing clearance makes the "squeeze film" effect more significant. The variation mechanism of displacement impedance with respect to bearing parameters is rather complex; both the pocket sizes and the shape have a great influence on the displacement impedance. As a result, an optimization is needed for searching the optimum displacement impedance.

5. Shape Optimization of the Air Pocket

To improve the bearing dynamic performances, both the self-excited characteristics and the displacement impedance should be considered. For suppression of the micro-vibration, R_e should be minimized for the bearing with an air pocket, and M_a should be less than 1 for the non-pocket or the small pocket bearing. The pocket volume is a key issue in happening of the pneumatic hammering vibration. It indicates that the volume of the pocket should be less than 5%-10% of the whole gas volume in the bearing clearance to avoid the pneumatic hammering [22]. Hence, the volume ratio is selected as one of the objective in optimization. Furthermore, the displacement impedance is considered as objectives in optimization. Improving the displacement impedance can greatly raise the load-resistance capability of the bearing [21]. Due to the fact that the main frequency ranges of the micro-vibration and the pneumatic hammering are at kHz-order [12, 16], and considering the fact that the bearing can resist the dynamic excitation with high frequencies effectively, the considered frequency range in optimization of the displacement impedance is selected as 0 Hz-2000 Hz; this frequency range is enough for optimization of the displacement impedance [21]. A series of frequency points are considered in 0 Hz-2000 Hz and the displacement impedance at these frequency points are maximized. In general, the optimization goal is to achieve the best dynamic behaviour under a given bearing load, and hence, the optimization model is established as follows:

$$\begin{aligned} &\max\ Z_{10}, Z_{30}, Z_{100}, Z_{300}, Z_{1000}, Z_{2000}, -R_e, \\ &s.t.\quad W = W_{load}, \\ &M_a < 1, \\ &vol_p / vol_w \le 5\%, \\ &(U - d)/2 \ge 0, \\ &x \in E, \end{aligned} \tag{6}$$

where W_{load} is the given bearing load, vol_p is the volume of the pocket, vol_w is the volume of the whole bearing clearance. Z_k is the displacement impedance at k Hz, and 6 frequency points are considered. $\boldsymbol{E}$ is the range of the design variables, and the design variables include: U, V_1, V_2, P_s, d. Each objective should be normalized firstly, and several give bearing loads are considered for comparison.

In the optimization, firstly the multi-island genetic algorithm is adopted. When using this method, the initial point is not required, and a more accurate global optimum point can be achieved. And then, the Hooke-Jeeves algorithm is considered based on the optimization results achieved in the first step. Hooke-Jeeves algorithm is a kind of direct search algorithm, and it is commonly used for searching an exacter optimum point after the application of the global optimization algorithm. The given bearing loads include: 80 N, 100 N, 120 N, and the optimization results are shown in Table 1.

Through optimization, the optimum shape and sizes of the air pocket are achieved. It can be seen that with increase of the given bearing load, the optimum air supply pressure increases and the air film thickness decreases,

Table 1

Optimization results

W_{given}, N	d, mm	P_s, MPa	U, mm	V_1, mm	V_2, mm	h, μm	M_a	R_e
80	0.105	0.450	0.219	0.060	0.087	12.8	0.72	2489
100	0.108	0.454	0.278	0.050	0.079	11.9	0.57	2468
120	0.190	0.455	0.198	0.126	0.075	9.4	0.61	914

which conforms to the general law. When the given load is small, the optimum orifice diameter nearly reaches the lower boundary, while when the given load increases, the optimum orifice diameter increases at the same time. The optimization results indicate that the combination of the cylinder pocket with a tapered inlet part is the best pocket configuration. With decrease of the air film thickness, the air-resistance is increased, and the gas mass flow rate is decreasing correspondingly, which induces the decrease of the Mach number and the Reynolds number.

Design optimization can also maximize the load-carrying capacity. When this load carrying capacity is set as the optimization objective, the optimal parameter combination is determined as follows: d = 0.19 mm, U = = 1.1 mm, V_1 = 0.05 mm, V_2 = 0.007 mm and P_s = 0.7 MPa. In this situation, the parameter V_2 nearly reaches the lower boundary, which means that an entirely cylindrical pocket is achieved, and also, a large orifice diameter, a large pocket diameter and a small pocket height are applied, respectively. In all cases, the constraint of the volume ratio is satisfied, which indicates that the pneumatic hammering is avoided. Moreover, the Reynolds number is minimized and the Mach number is less than 1, which means that the micro-vibration is reduced or eliminated.

6. Conclusion

The dynamic performances of the aerostatic bearing are concentrated and the air pocket shape is optimized. The micro-vibration and the pneumatic hammering vibration are both reduced to enhance the bearing operational stability. And also, the displacement impedance of the air film-floating facility system is optimized to improve the capability of the bearing to resist the dynamic load. The following conclusions can be drawn:

For the aerostatic bearing without an air pocket or with a small air pocket, the flow structures are similar. The occurrence of the supersonic region may induce the shock waves, and thereby, the separation of boundary layer happens and the vortex flow forms. For the bearing with a large cylindrical or tapered pocket, the vortex flow always exists in the air pocket. Because the occurrence of the vortex flow may cause the pressure fluctuation and thus inducing the micro-vibration, the maximum Mach number in the air film and the Reynolds number at the inlet of the pocket should both be considered in optimization to suppress the vortex flow, and thereby reducing the micro-vibration. The pocket volume should be restricted to avoid the occurrence of the pneumatic hammering.

The displacement impedance directly reflects the capability of the bearing to resist the external dynamic load. It increases notably with the excitation frequency, which means that the bearing can resist the external load with high excitation frequency effectively. To improve the dynamic behaviour of the bearing, the displacement impedance should be considered as an objective in optimization.

The dynamic performances are improved through shape optimization. The displacement impedance, Reynolds number are taken as design objectives, and the given bearing load, the maximum Mach number, as well as the volume ratio are considered as design constraint. The results show that the combination of a cylinder pocket with a tapered inlet part is the best pocket configuration. While for maximizing the load carrying capacity, an entirely cylindrical pocket is proper.

Acknowledgement

The work described in this paper was financially supported by the National Natural Science Foundation of China “Study on stability and air-tightness performance of abandoned mine cavern for compressed air storage and reliability evaluation” (No. U24A20599).

Funding

This research was funded by the National Natural Science Foundation of China “Study on stability and air-tightness performance of abandoned mine cavern for compressed air storage and reliability evaluation ” (No. U24A20599).

References

1. **Li, Y. T.; Ding, H.** 2012. A simplified calculation method on the performance analysis of aerostatic thrust bearing with multiple pocketed orifice-type restrictors, Tribology International 56: 66-71. https://doi.org/10.1016/j.triboint.2012.06.018.
2. **Li, Y. T.; Ding, H.** 2007. Influences of the geometrical parameters of aerostatic thrust bearing with pocketed orifice-type restrictor on its performance, Tribology International 40(7): 1120-1126. https://doi.org/10.1016/j.triboint.2006.11.001.
3. **Belforte, G.; Colombo, F.; Raparelli, T.; Trivella, A.; Viktorov, V.** 2010. Performance of Externally Pressurized Grooved Thrust Bearings, Tribology letters 37: 553-562. https://doi.org/10.1007/s11249-009-9550-3.
4. **Belforte, G.; Raparelli, T.; Trivella, A.; Viktorov, V.; Visconte, C.** 2015. CFD Analysis of a Simple Orifice-Type Feeding System for Aerostatic Bearings, Tribology Letters 58: 25. https://doi.org/10.1007/s11249-015-0503-8.
5. **Arghir, M.; Matta, P.** 2009. Compressibility effects on the dynamic characteristics of gas lubricated mechanical components, Comptes Rendus Mécanique 337(11-12): 739-747. https://doi.org/10.1016/j.crme.2009.09.002.
6. **Boffey, D. A.** 1978. A Study of the Stability of an Externally-Pressurized Gas-Lubricated Thrust Bearing With a Flexible Damped Support, ASME Journal of Lubrication Technology 100(3): 364-368. https://doi.org/10.1115/1.3453186.
7. **Bhat, N.; Kumar, S.; Tan, W.; Narasimhan, R.; Low T. C.** 2012. Performance of inherently compensated flat pad aerostatic bearings subject to dynamic perturbation forces, Precision Engineering 36(3): 399-407. https://doi.org/10.1016/j.precisioneng.2012.01.002.
8. **Chen, X. D.; Zhu, J. C.; Chen, H.** 2013. Dynamic characteristics of ultra-precision aerostatic bearings, Advances in Manufacturing 1: 82-86. https://doi.org/10.1007/s40436-013-0013-6.
9. **Chen, X. D.; Chen, H.; Luo, X.; Ye, Y. X.; Hu, Y. T.; Xu, J. Q.** 2011. Air vortices and nano-vibration of aerostatic bearings, Tribology Letters 42: 179-183.

https://doi.org/10.1007/s11249-011-9761-2.
10. **Zhu, J. C.; Chen, H.; Chen, X. D.** 2013. Large eddy simulation of vortex shedding and pressure fluctuation in aerostatic bearings, Journal of Fluids and Structures 40: 42-51. https://doi.org/10.1016/j.jfluidstructs.2013.03.012.
11. **Talukder, H. M.; Stowell, T. B.** 2003. Pneumatic hammer in an externally pressurized orifice-compensated air journal bearing, Tribology International 36(8): 585-591. https://doi.org/10.1016/S0301-679X(02)00247-5.
12. **Li, Y. T.; Zhao, J. Y.; Zhu, H. X.; Lin, Y. X.** 2015. Numerical analysis and experimental study on the microvibration of an aerostatic thrust bearing with a pocketed orifice-type restrictor, Proceedings of the Institution of Mechanical Engineers, Part J: Journal of Engineering Tribology 229(5): 609-623. https://doi.org/10.1177/1350650114556556.
13. **Aoyama, T.; Kakinuma, Y.; Kobayashi, Y.** 2006. Numerical and Experimental Analysis for the Small Vibration of Aerostatic Guideways, CIRP Annals-Manufacturing Technology 55(1): 419-422. https://doi.org/10.1016/s0007-8506(07)60449-1.
14. **Li, Y. F.; Yin, Y. H.; Yang, H.; Liu, X. E.; Mo, J.; Cui, H. L.** 2017. Modeling for optimization of circular flat pad aerostatic bearing with a single central orifice-type restrictor based on CFD simulation, Tribology International 109: 206-216. https://doi.org/10.1016/j.triboint.2016.12.044.
15. **Ye, Y. X.; Chen, X. D.; Hu, Y. T.; Luo, X.** 2010. Effects of recess shapes on pneumatic hammering in aerostatic bearings, Proceedings of the Institution of Mechanical Engineers, Part J: Journal of Engineering Tribology 224(3): 231-237. https://doi.org/10.1243/13506501JET664.
16. **Gao, S. Y.; Cheng, K.; Chen, S. J.; Ding, H.; Fu, H. Y.** 2015. CFD based investigation on influence of orifice chamber shapes for the design of aerostatic thrust bearings at ultra-high speed spindles, Tribology International 92: 211-221. https://doi.org/10.1016/j.triboint.2015.06.020.
17. **Wang, N.; Cha, K. C.** 2010. Multi-objective optimization of air bearings using hypercube-dividing method, Tribology International 43(9): 1631-1638. https://doi.org/10.1016/j.triboint.2010.03.009.
18. **Bhat, N.; Barrans, S. M.; Kumar, A. S.** 2010. Performance analysis of Pareto optimal bearings subject to surface error variations, Tribology International 43(11): 2240-2249. https://doi.org/10.1016/j.triboint.2010.07.012.
19. **Fesanghary, M., Khonsari, M. M.** 2013. On the optimum groove shapes for load-carrying capacity enhancement in parallel flat surface bearings: theory and experiment, Tribology International 67: 254-262. https://doi.org/10.1016/j.triboint.2013.08.001.
20. **Yu, P. L.; Chen, X. D.; Wang, X .L.; Jiang, W.** Frequency-dependent nonlinear dynamic stiffness of aerostatic bearings subjected to external perturbations, International journal of precision engineering and manufacturing 16: 1771-1777. https://doi.org/10.1007/s12541-015-0232-9.
21. **Li, Y. F.** 2023. Investigation of micro-vibration reduction method based on dynamic performance analysis of aerostatic bearing, Proceedings of the Institution of Mechanical Engineers, Part J: Journal of Engineering Tribology 237: 2074–2087. https://doi.org/10.1177/13506501231198288.
22. **Wang, Y. F.** 1999. Gas lubrication theory and gas bearing design, China Machine Press, Beijing. (in Chinese).

Y. Li

SHAPE OPTIMIZATION OF THE AEROSTATIC BEARING CONSIDERING DYNAMIC PERFORMANCES

S u m m a r y

The shape optimization is conducted to improve the dynamic performances of the aerostatic bearing with an air pocket. Firstly, the basic configuration of the air pocket used in the optimization is created, and four typical flow patterns are discussed. And then, the displacement impedance of the air film-floating facility system is studied, and the effects of bearing parameters on displacement impedance are discussed in detail. The approximate model of the displacement impedance is established; the optimization model is built based on the flow analysis, and both the Reynolds number and the maximum Mach number in the bearing clearance are considered in optimization to suppress the micro-vibration. The shape optimization is conducted and the optimum pocket configuration is achieved. Through optimization, the self-excited vibration is reduced, and the capability of the bearing to resist the external dynamic load is enhanced, which means that the operational stability of the aerostatic bearing is improved. The optimization process offers a reference for the bearing optimization in the engineering application.

Keywords: self-excited vibration, displacement impedance, aerostatic bearing, numerical simulation.

Received March 23, 2024
Accepted February 21, 2025